frontiers in Chemical Engineering

ORIGINAL RESEARCH
published: 04 March 2021
doi: 10.3389/fceng.2021.636439

Bimetallic Coordination in Two-Dimensional Metal–Organic Framework Nanosheets Enables Highly Efficient Removal of Heavy Metal Lead (II)

Guiliang Li[1,2], *Yang Liu*[1,2], *Yi Shen*[3], *Qile Fang*[1,2]* *and Fu Liu*[1,2]*

[1]*Key Laboratory of Marine Materials and Related Technologies, Zhejiang Key Laboratory of Marine Materials and Protective Technologies, Ningbo Institute of Materials Technology and Engineering, Chinese Academy of Sciences, Ningbo, China,* [2]*Department of Chemical Science, University of Chinese Academy of Sciences, Beijing, China,* [3]*Key Laboratory of Microbial Technology for Industrial Pollution Control of Zhejiang Province, College of Environment, Zhejiang University of Technology, Hangzhou, China*

Two-dimensional (2D) metal–organic frameworks (MOFs) have emerged as intriguing 2D materials because of their specific features of 2D morphology and designable skeletons, which have elicited great interest in environment remediation. In this work, 2D MOF nanosheets are fabricated *via* a mixed-solvent solvothermal method, and a regulation strategy of metal inorganic clusters on MOFs is used to construct two different 2D MOFs with monometallic and bimetallic coordination, that is, Ni-MOF and Ni/Cd-MOF. Binary metal coordination renders more crystal defects and vacancies in the framework; thus, compared to monometallic Ni-MOF, bimetallic Ni/Cd-MOF exhibits fewer layers (4~5 layers), higher specific surface area, larger pore size, and higher surface electronegativity, which leads to its excellent adsorption removal for Pb^{2+}, with higher adsorption rate and affinity, and superior adsorption capacity (950.61 mg/g, almost twice as high as that of monometallic Ni-MOF). Besides, the adsorption mechanism further confirmed that the carboxyl groups (–COO–) from organic linker on 2D MOFs serve as the main binding sites for Pb^{2+} coordination, and bimetallic Ni/Cd-MOF has more active –COO– sites for Pb^{2+} capture. Thus, the bimetallic Ni/Cd-MOF regulated by heterogeneous metal atoms shows promising application for highly efficient adsorption of heavy metal ions.

Keywords: bimetallic, two dimensional, metal–organic frameworks, heavy metal ion removal, nanosheet

OPEN ACCESS

Edited by:
Zhigang Hu,
Brunel University London,
United Kingdom

Reviewed by:
Ludovic Francis Dumée,
Deakin University, Australia
Junkuo Gao,
Zhejiang Sci-Tech University, China

***Correspondence:**
Qile Fang
fangqile@nimte.ac.cn
Fu Liu,
fu.liu@nimte.ac.cn

Specialty section:
This article was submitted to Separation Processes, a section of the journal Frontiers in Chemical Engineering

Received: *01 December 2020*
Accepted: *25 January 2021*
Published: *04 March 2021*

Citation:
Li G, Liu Y, Shen Y, Fang Q and Liu F (2021) Bimetallic Coordination in Two-Dimensional Metal–Organic Framework Nanosheets Enables Highly Efficient Removal of Heavy Metal Lead (II). Front. Chem. Eng. 3:636439. doi: 10.3389/fceng.2021.636439

INTRODUCTION

Water pollution poses a great challenge to the sustainable development of human society, and organic pollutants and heavy metal ions are the biggest culprits, of which heavy metal ions are of special concern ascribing to their recalcitrance in the environment (Chen and Wang, 2006). For example, the heavy metal ion of lead (Pb^{2+}), which is nonbiodegradable, could accumulate in living organisms and cause damage to the central nervous system, liver, and reproductive system. In particular, exposure to lead could cause irreversible effects in terms of the cognitive performance of children (Naseem and Tahir, 2001; Fu and Wang, 2011). Therefore, control and management of heavy metal ions in case they are released into the environment as a growing burden of pollution are vitally important and urgent. Among the mature techniques [e.g., chemical precipitation (Matlock

and Howerton, 2002), ion exchange (Alyüz and Veli, 2009), adsorption (Yang et al., 2011), and membrane filtration (Liu et al., 2020)], adsorption is an appealing treatment option because of its high efficiency and low energy (Li et al., 2019b). Great efforts have been devoted to exploring high-efficient adsorbent materials such as bimetallic oxide (Wen et al., 2018) and porous carbon (Jafari et al., 2020). In recent years, framework-based materials with abundant porous structures and functional surface groups have gained great concerns and considered to be burgeoning adsorbents (Li et al., 2018; Duan et al., 2019).

One of the attention-grabbing framework-based nanomaterials, metal–organic framework (MOF) materials with predesigned structure and active sites, has been widely applied in water purification (Jiang et al., 2019), carbon dioxide reduction (Meng et al., 2020; Yan et al., 2020), sensors (Li et al., 2016), *etc*. However, porous and function-customized characteristics make MOFs excellent candidates as adsorbents to remove heavy metal ions with superior performances (Chen et al., 2016; Lei et al., 2019; Zhang et al., 2020). To date, a series of MOFs such as UiO-66 (Luo et al., 2016), ZIF-8 (Jian et al., 2016), and MIL-101 (Luo et al., 2015b) have been reported for the adsorption of heavy metal ions. MOFs were constructed with two main components: the metal inorganic clusters and the organic linkers, where the linkers acting as "struts" connect the "joints" of metal ions (Abednatanzi et al., 2019). Usually, organic linkers are the processing targets to design functional MOFs to boost adsorption performance; for example, adopting large organic linkers enables larger pore size of MOFs to facilitate adsorption diffusion (Vuong et al., 2013), and decorating organic linkers with targeted groups [-NH_2 (Howarth et al., 2015), -OH (Luo et al., 2015a), *etc*.] offers more effective sites to increase adsorption capacity or improve adsorption selectivity. Only a few works have been involved in the regulation strategy about metal inorganic clusters for pollutant removal. Zhang and coworkers prepared an Fe/Mn bimetal–organic framework for efficient As(III) removal, with doubled adsorption capacity (161.6 $mg{\cdot}g^{-1}$) compared to monometallic Fe-MOF (Zhang et al., 2019), and Yang and coworkers synthesized Mn-doped UiO-66, which exhibited 3.1 times higher adsorption capacity for Cr(VI) removal than pristine UiO-66 (Yang et al., 2019). The effect of metal inorganic cluster regulation on improving adsorption capacity is remarkable, but very limited information can be obtained about the mechanism and regulatory rule, especially for those heavy metal ions with nonoxidative/nonreductive activity. In principle, it is thought that mixed-metal MOFs can offer several advantages over monometallic MOFs by providing complexity and introducing functionality derived from the different metal ions in the MOF structure, and it is predicted that the adsorption performance of mixed-metal MOFs will be beyond that achieved by homometallic MOFs (Abednatanzi et al., 2019; Masoomi et al., 2019).

Two-dimensional (2D) MOFs with 2D morphology and high lateral area-to-thickness aspect ratio (Peng et al., 2014; Zhao et al., 2018; Li et al., 2019a) can expose every active site on their surface that is available to pollutants without diffusion limitations, and this obvious advantage with respect to the three-dimensional counterparts makes 2D MOFs a rapidly growing concern in the field of water purification (Xu et al., 2018; Dhakshinamoorthy et al., 2019; Xu et al., 2020). Structural regulation or post-modification based on 2D MOFs is important to achieve its high adsorption performance for pollutant removal. Hence, in this work, 2D MOF nanosheets were fabricated *via* a one-step solvothermal method, and the strategy of coordinate metal ions regulation was used to construct two different 2D MOFs with monometallic and bimetallic coordination. The morphology and structural properties of the two as-prepared 2D MOFs were comparatively studied, and their adsorption capacities for Pb^{2+} removal were comparatively researched. Bimetallic Ni/Cd-MOF shows an excellent adsorption removal of Pb^{2+}, with a higher adsorption rate, higher adsorption affinity, and superior adsorption capacity, than the monometallic Ni-MOF. Furthermore, the adsorption mechanism based on bimetallic coordination for improving Pb^{2+} removal on 2D MOFs was deeply studied, and the results gleaned here would provide valuable guidance in the 2D MOF material design for efficiently removing heavy metal ions.

MATERIALS AND METHODS

Chemicals and Materials

Nickel(II) acetate tetrahydrate ($Ni(OAc)_2{\cdot}4H_2O$), terephthalic acid (1,4-H_2BDC), ethanol, and N,N-dimethylacetamide (DMAC) were purchased from Sinopharm Chemical Reagent Co., Ltd. Cadmium(II) sulfate ($CdSO_4{\cdot}8/3H_2O$) and lead nitrate ($Pb(NO_3)_2$) were purchased from Aladdin Biochemical Technology Co., Ltd. All chemicals were used without further purification.

2D MOF Preparation

Bimetallic Ni/Cd-MOF was prepared *via* a method of one-step hydrothermal reaction. In brief, a solution composed of 0.25 mmol $Ni(OAc)_2{\cdot}4H_2O$ and 0.075 mmol $CdSO_4{\cdot}8/3H_2O$ dissolved in 30 ml deionized (DI) water was prepared. Then, another solution with 0.125 mmol 1,4-H_2BDC in 30 ml DMAC was well mixed with the former Ni/Cd mixture solution to obtain a homogeneous mixture, which was transferred to a 100-ml Teflon vessel subsequently, and sealed to heat at 150°C for 3 h. After the reaction, light green powder was collected by filtration when the mixture was cooled to room temperature. Finally, the precipitate was washed three times alternately by ethanol and DI water and dried at 80 C overnight. The same process was used to prepare monometallic Ni-MOF, and the only variable is that only 0.25 mmol $Ni(OAc)_2{\cdot}4H_2O$ and no 0.075 mmol $CdSO_4{\cdot}8/3H_2O$ are added to the metal salt solution compared to Ni/Cd-MOF.

Characterization of 2D MOFs

The morphologies of the obtained MOFs were characterized by scanning electron microscopy (SEM) with a Hitachi S4800 cold field emission (Japan) and transmission electron microscopy (TEM, Tecnai F20, Japan) equipped with selected area electron diffraction (SEAD). Scanning probe microscope (SPM, Dimension 3100, Vecco, United States, containing AFM

function) was used to measure the thickness of MOF nanosheets. The samples were examined by X-ray diffractometer (D8 ADVANCE, Bruker, Germany) with a Cu Kα X-ray source at 2θ of 5-40°. Structural information and chemical composition were characterized using Fourier transform infrared spectral (FTIR, Thermo Nicolet 6700, United States), Raman (Renishaw inVia reflex, United Kingdom), and X-ray photoelectron spectrometer (XPS, Axis Ultra DLD, Kratos, Japan) [among them, the XPS peaks were calibrated using contaminated carbon (284.6 eV) as a benchmark], respectively. Automatic gas adsorption analyzer (ASAP2020HD88, Micromeritics, United States) was used to test the specific surface area and pore size distribution of the absorbents, and the degassed temperature of the Ni-based MOFs was at 120°C for 6 h, whose surface charges at different pH were measured by Nano-ZS Zetasizer (Malvern, United Kingdom).

Adsorption Experiments

Under an initial Pb^{2+} concentration of 300 mg/L, the effect of solution pH on Pb^{2+} adsorption was performed on Ni-MOF and Ni/Cd-MOF with a solid–liquid ratio of 5 mg/15ml, and the solution pH value was adjusted ranging from 2.5 to 7. The equilibrium pH values were recorded, and Pb^{2+} concentration was detected after 12 h of adsorption at 100 rpm, room temperature. The adsorption kinetics experiments for 2D MOFs were similarly carried out at an initial Pb^{2+} concentration of 300 mg/L without solution pH adjustment, and Pb^{2+} concentration was monitored at different time intervals. A batch equilibrium method was conducted for the isothermal adsorption experiments with the initial Pb^{2+} concentration ranging from 0 to 900 mg/L; after 12 h of adsorption, the apparent equilibrium concentration of Pb^{2+} at every point was measured, and then, isothermal curves were drawn. All experiments were tested twice. Pb^{2+} concentration in this work was analyzed by an inductively coupled plasma emission spectrometry (ICP-OES, SPECTROARCOS II, Germany). The specific adsorption amount (q) and remove rate (R) of Pb^{2+} were calculated by **Eq. 1** and **Eq. 2**:

$$q = (C_o - C_e) \times V/m. \quad (1)$$

$$R = (C_o - C_e)/C_o \times 100\%. \quad (2)$$

$$K_d = q/C_e. \quad (3)$$

where C_o and C_e are the initial concentration and equilibrium concentration of Pb^{2+}(mg/L), respectively, V is the volume of the added solution (ml), m is the weight of the added adsorbents(mg), and K_d is the partition coefficient of Pb^{2+} (L/mg).

RESULTS

Synthesis and Characterization of Ni-MOF and Ni/Cd-MOF

A bottom-up solvothermal method using mixed solvent was used to synthesize 2D MOFs, with terephthalic acid as the organic linker and predesigned metal ions as the connecting "joints" (Li et al., 2019a). Regulation of metal ions in 2D MOFs was realized by a monometallic Ni source and bimetal Ni/Cd sources. Morphologies and microstructures of the resulted MOFs were investigated by SEM, TEM, and AFM. From **Figures 1A,D**, the typical lamellar structure can be observed on both Ni-MOF and Ni/Cd-MOF, with a large lateral size of about 2 μm. Given simple ultrasonic dispersion in sample preparation for TEM characterization, the two obtained MOFs present transparent sheet appearance in **Figures 1B,E**, indicating an ultrathin thickness of them. The crystalline property of the 2D MOFs can be preliminarily revealed from the concentric ring patterns of selected area electron diffraction (SEAD), independent of monometallic or bimetallic coordination. Subsequently, AFM was used to measure the lamellar thickness, as shown in **Figures 1C,F**, and bimetallic Ni/Cd-MOF nanosheet was characterized with an average thickness of ~ 4.6 nm, thinner than monometallic Ni-MOF of ~ 5.7 nm thickness. The elemental composition and distribution of the 2D MOF nanosheets were further verified by EDX in **Figures 1G,H**. Homogeneous bimetal distributions of Ni and Cd are found on Ni/Cd-MOF nanosheets, different from the monometallic Ni-MOF with only metal Ni mapping. The two as-prepared 2D MOFs also exhibited their excellent dispersion in an aqueous solution, reflecting the obvious Tyndall effect in **Figure 1I**. Thus, monometallic and bimetallic 2D MOF ultrathin nanosheets were successfully and directly fabricated *via* the mixed-solvent solvothermal method, without further exfoliation (Peng et al., 2014; Cliffe et al., 2017; Pang et al., 2020), and the gram-scale yield makes the method feasible to achieve large-scale production, as shown in **Supplementary Figure S1**.

Framework chemical structures of the prepared 2D MOFs were confirmed *via* FTIR and Raman spectra in **Figures 2A,B**, and **Supplementary Figure S2**. Compared to organic monomer 1,4-H_2BDC with a single band at 1,682 cm^{-1} (asymmetrical stretching vibration of carboxyl, –COO–), obvious double bands of asymmetrical (1,574 cm^{-1}) and symmetrical (1,378 cm^{-1}) stretching vibrations of –COO– can be found on both Ni-MOF and Ni/Cd-MOF. What is more, the intensity ratio of benzene ring vibration to –COO– symmetrical stretching vibration ($I_{\text{benzene ring}}/I_{-COO-}$) changes significantly in Raman spectra (**Figure 2B**), decreasing from 5.27 of monomer to 1.27 of Ni-MOF and 1.18 of Ni/Cd-MOF. All the information reveals a bidentate mode of –COO– on 1,4-H_2BDC coordinated with metal ions in the 2D MOF framework (Li et al., 2019a). The significant blue-shift phenomenon of the out-of-plane bending vibration peaks of C–H in the benzene ring occurred on the organic linker after coordination with metal, which blue-shifted from 730 cm^{-1} and 782 cm^{-1} of 1,4-H2BDC to 758 cm^{-1} and 812 cm^{-1} of Ni/Cd-MOF and 750 cm^{-1} and 817 cm^{-1} of Ni-MOF, respectively (**Supplementary Figure S2**), manifesting such that coordination rendered a decrease of delocalized electron cloud density on the benzene ring of 1,4-H_2BDC and increased its vibration energy. Besides, Cd-O/Ni-O bimodal vibration peaks in Ni/Cd-MOF displayed around 420–480 cm^{-1}, which is in stark contrast to the unimodal peak (Ni-O) in Ni/MOF (Li et al., 2019a; Wang et al., 2015; Caglayan and Aksoylu, 2013; Uzunova et al., 1994). Chemical compositions of the 2D MOFs were further analyzed by X-ray photoelectron spectroscope (XPS). According

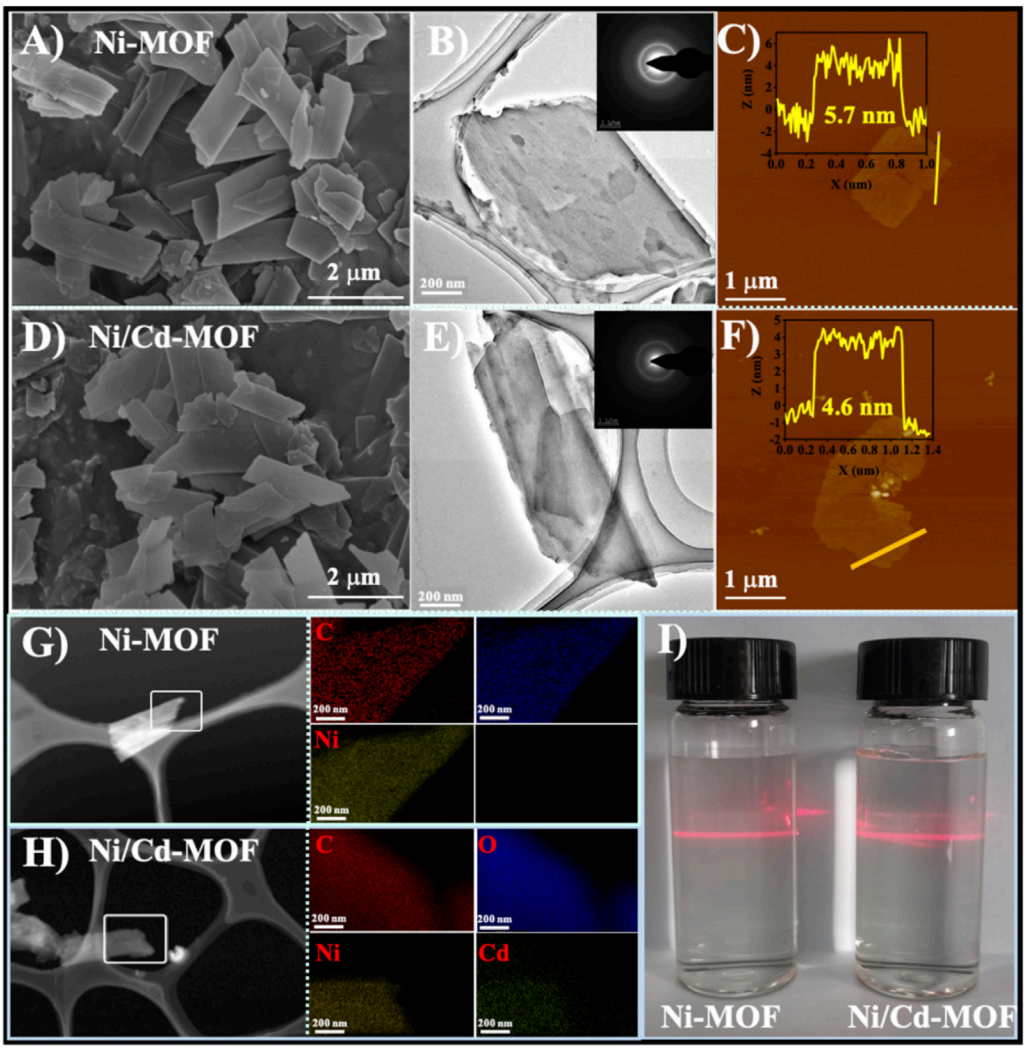

FIGURE 1 | (A) SEM, **(B)** TEM, and **(C)** AFM images of Ni-MOF, the inset is the corresponding SAED pattern; **(D)** SEM, **(E)** TEM, and **(F)** AFM images of Ni/Cd-MOF; STEM image and EDX elemental mappings of **(G)** Ni-MOF and **(H)** Ni/Cd-MOF; **(I)** Tyndall effect of Ni-MOF and Ni/Cd-MOF in aqueous solution.

to the full XPS spectra in **Figure 2C**, the Ni/Cd atom ratio of the bimetallic 2D MOF was calculated to be 2.21, close to the theoretical value of 2, which signifies a controllable method adopted in this study for metal inorganic cluster regulation on MOFs. The peak-differentiating analysis was carried out for Ni and Cd elements as shown in **Figures 2E–G**. High-resolution XPS spectra of Ni 2p can be deconvoluted into four peaks on both Ni-MOF and Ni/Cd-MOF, among which the peaks at 876.3 eV and 856.0 eV are assigned to Ni $2p_{3/2}$ and Ni $2p_{1/2}$, respectively, and the remaining two are satellite peaks. These signals verify an oxidation state (+2) of the Ni element in the coordination framework (Du et al., 2019). On the bimetallic Ni/Cd-MOF sample, two characteristic peaks located at 411.6 eV ($3d_{3/2}$) and 404.9 eV ($3d_{5/2}$) can be deconvoluted from its Cd 3d XPS spectrum specifically.

Wide-angle XRD tests were carried out on the 2D MOFs. As displayed in **Figure 2D**, the XRD patterns of both Ni-MOF and Ni/Cd-MOF were in good accordance with that of nickel hydroxide terephthalate hydrate (JCPDS No.035-1677), reflecting that the main crystal structure was maintained well on the 2D MOFs albeit with an inorganic metal regulation. However, a slight shift of the (003) and (006) diffraction peaks at 12.3°, 28.8° of Ni-MOF can be observed to lower angles at 11.8°, 28.1°of bimetallic Ni/Cd-MOF (Cai et al., 2020). Together with the broadening and weakening trend, the changes on these two diffraction peaks indicate more crystal defects in Ni/Cd-MOF. Meanwhile, based on the Bragg equation, interlayer spacing was calculated according to (2 0 0) facet to be 0.9408 nm for Ni-MOF, smaller than the value of 1.0048 nm of Ni/Cd-MOF, and the incorporation of Cd with a larger atomic radius (1.57 Å) than Ni (1.24 Å) accounts for enhanced interlayer spacing. Hence, combining with the thickness detected by AFM, there are 4~5 layers in Ni/Cd-MOF nanosheets and ~6 layers in Ni-MOF nanosheets. Based on the above composition and structure

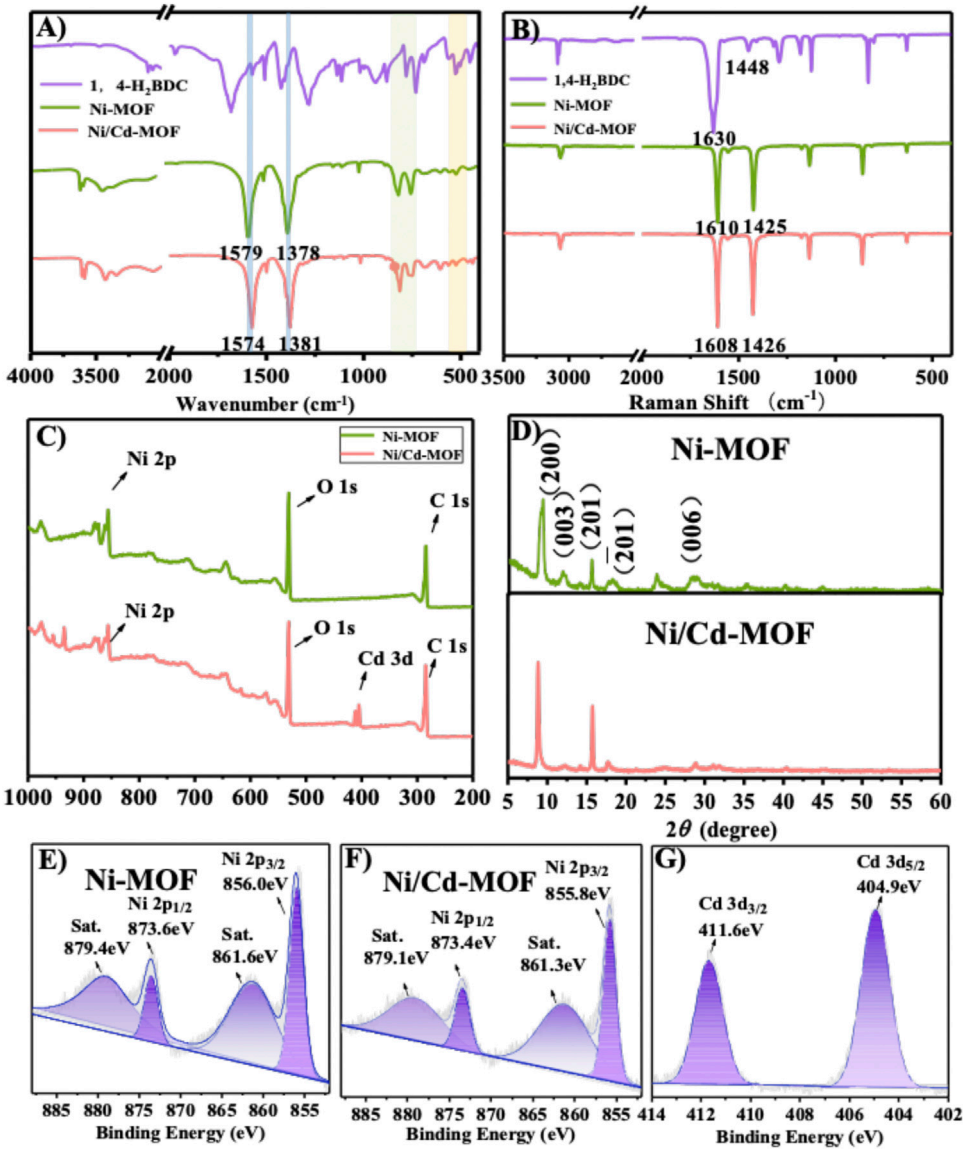

FIGURE 2 | (A) FTIR and **(B)** Raman spectra of Ni-MOF, Ni/Cd-MOF, and 1,4-H_2BDC; **(C)** XPS full spectra of Ni-MOF and Ni/Cd-MOF; **(D)** XRD patterns of Ni-MOF and Ni/Cd-MOF; **(E)** Ni 2p spectra of Ni/MOF; **(F)** Ni 2p; and **(G)** Cd 3d spectra of Ni/Cd-MOF.

analysis, framework structures of the as-prepared monometallic and bimetallic 2D MOFs are illustrated in **Figure 3**.

The specific surface area and porosity of the 2D MOFs were further explored by N_2 adsorption–desorption tests (**Figure 4**). According to the Brunauer–Emmet–Teller (BET) theory (**Figure 4A**), a specific surface area of 35.37 m^2/g was detected for bimetallic Ni/Cd-MOF, three times higher that that of monometallic Ni-MOF, with the value of 10.97 m^2/g. Considering the double atomic mass of Cd with respect to Ni, the increase of surface area by bimetallic coordination in 2D MOFs should be higher in terms of molar equivalent. It is thought that more vacancies might be created in the framework when a second metal ion was introduced, which includes lattice distortion and locally unbalanced coordination, consequently resulting in higher porosity or higher lamellar charge (Vuong et al., 2013). Consistent with it, the pore distribution of Ni/Cd-MOF is mainly concentrated at ~2.6 nm (**Figure 4B**), larger than homometallic Ni-MOF (~2.0 nm).

Pb^{2+} Adsorption Onto Ni-MOF and Ni/Cd-MOF

Structural stability in an aqueous solution is a prerequisite to ensure the adsorption application of 2D MOFs for heavy metal ion removal. The changes in morphology and crystal structure of the as-prepared 2D MOFs at different pH solutions were investigated by SEM and XRD, respectively. **Figures 5A,B** show that typical lamellar structures of Ni-MOF and Ni/Cd-MOF are

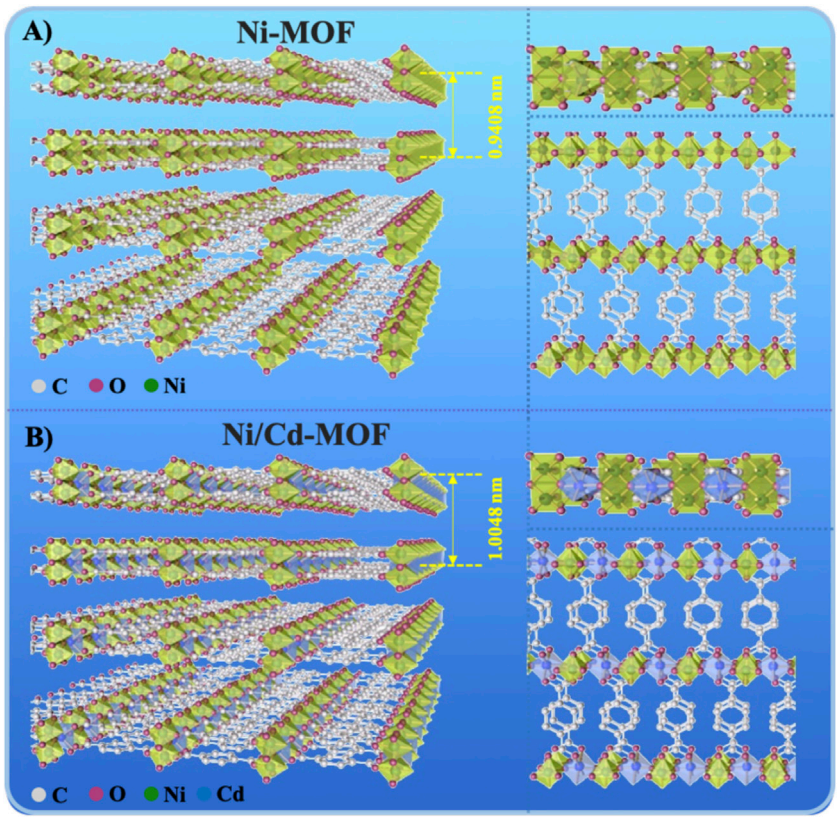

FIGURE 3 | Structure schematic diagram of **(A)** Ni-MOF and **(B)** Ni/Cd-MOF.

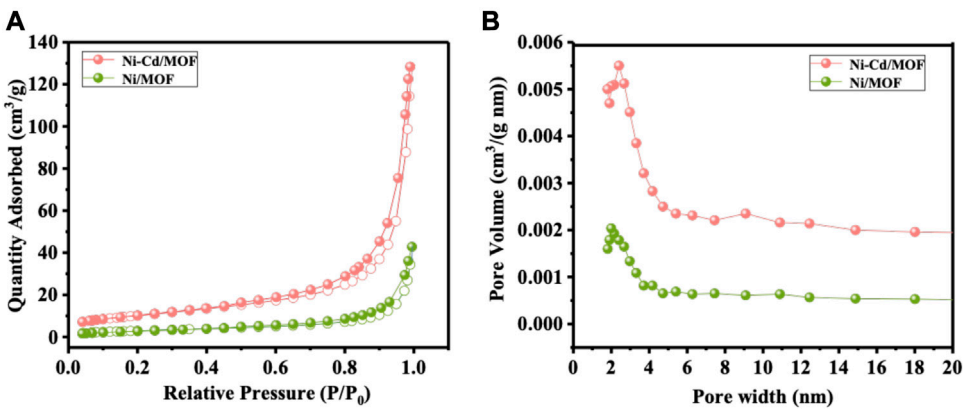

FIGURE 4 | (A) N_2 adsorption and desorption isotherms; **(B)** pore size distribution of Ni-MOF and Ni/Cd-MOF.

well maintained at pH about 2, 4.5, and 7.5. The XRD results (**Figures 5C,D**) also demonstrate a complete crystal structure of 2D MOFs at pH 4.5 and 7.5 but slight crystal collapse in extremely acidic conditions (pH of 2). Similar to most other MOF materials, Ni-MOF and Ni/Cd-MOF have unstable frameworks in strong alkaline solutions, which caused 2D MOFs to dissolve, and the weak Tyndall phenomenon of their nanosheets can be seen in **Figures 5E,F**. However, the pH range of application of the two 2D MOFs was exactly in line with the pH range of Pb with ionic species. As is well known, heavy metal ions with various species usually have different adsorption behaviors, significantly dependent on the solution pH value. The species distribution of Pb at different pH is displayed in **Figure 6A** and **Supplementary Table S1**. Pb with ionic species [Pb^{2+} and $Pb(OH)^{+}$] are mainly

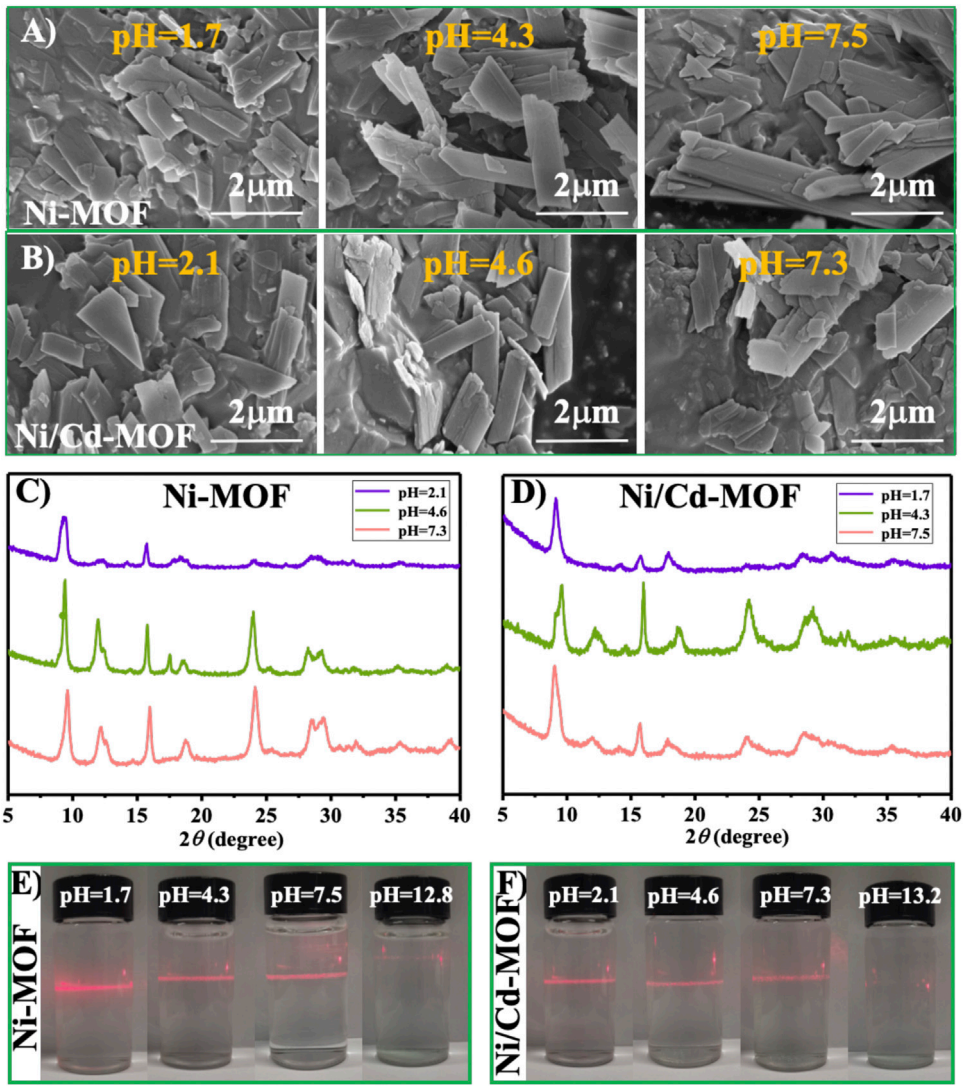

FIGURE 5 | SEM images of **(A)** Ni-MOF and **(B)** Ni/Cd-MOF at different pH; XRD patterns of **(C)** Ni-MOF and **(D)** Ni/Cd-MOF at different pH; Tyndall effect of **(E)** Ni-MOF and **(F)** Ni/Cd-MOF in aqueous solutions with different pH.

located at pH below 8; thus, adsorption behaviors of Pb on the two as-prepared 2D MOFs were examined in a pH range of 2.5~7.5 with Pb^{2+} as the principal specie.

As shown in **Figure 6B**, Pb^{2+} adsorption is greatly sensitive to aqueous pH, and increased pH leads to a drastic improvement for Pb^{2+} adsorption on the two 2D MOF materials. For example, the absorbed amount of Pb^{2+} on Ni-MOF increased from 43.2 mg/g at pH 2.9 to 1,011.5 mg/g at pH 7.2, and more significantly, in the case of bimetallic Ni/Cd-MOF, the absorbed amount of Pb^{2+} increased from 50.2 mg/g at pH 2.8 to 1,495.2 mg/g at pH 6.9. It is clear that Ni/Cd-MOF exhibited a higher adsorption capacity for Pb^{2+} removal than monometallic Ni-MOF over the test pH range. Surface charge was characterized by Zeta potential to explore the performance difference between monometallic and bimetallic 2D MOFs. According to the result in **Figure 6C**, the 2D MOF surfaces were almost negatively charged at the whole test pH range, excepting the first point around pH 2.5. In detail, the Zeta potential of Ni/Cd-MOF decreased from 1.75 mV at pH 2.6 to -10.65 mV at pH 6.8, wholly lower than Ni-MOF which decreased from 1.05 mV at pH 2.8 to -7.7 mV at pH 6.7. The increasing negative charge on 2D MOF sheets with the increase of solution pH contributed to a rising electrostatic attraction for positive Pb^{2+} binding. In addition, more negative charges on bimetallic Ni/Cd-MOF derived from locally unbalanced coordination make it higher adsorption capacity for Pb^{2+} removal. Moreover, higher electrostatic repulsion between Ni/Cd-MOF monolayers causes less stacking of Ni/Cd-MOF (4~5 layers) in the resulted lamellar structure, compared with monometallic Ni-MOF.

In order to further explore the adsorption behavior of Pb^{2+} on Ni-MOF and Ni/Cd-MOF, adsorption kinetic experiments were

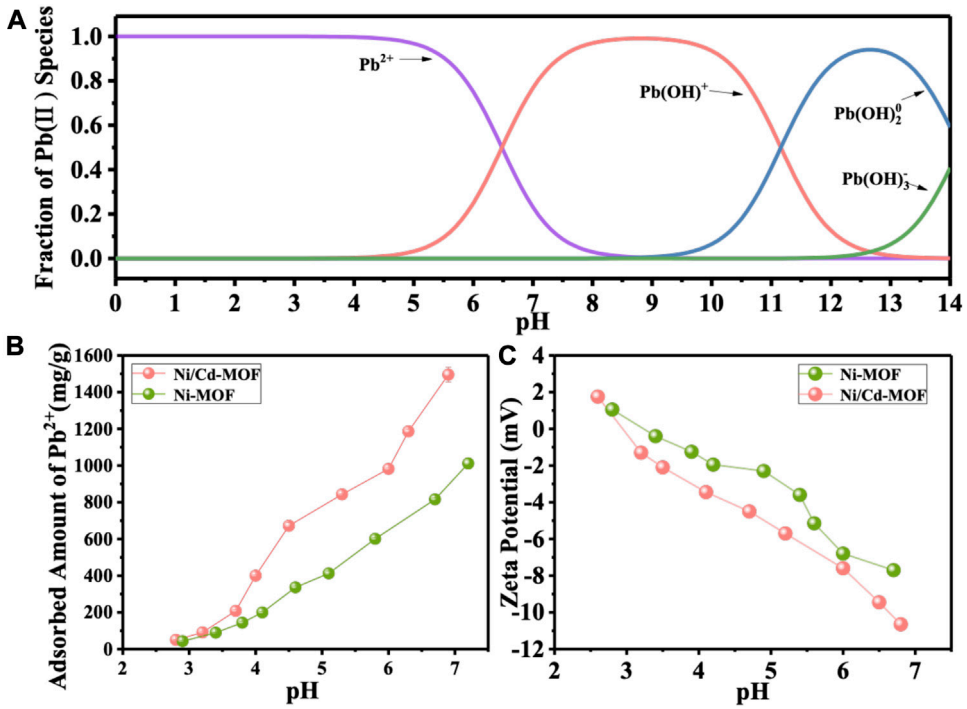

FIGURE 6 | (A) Fraction of Pb(II) species at different pH solution; **(B)** adsorption of Pb^{2+} by Ni-MOF and Ni/Cd-MOF at different pH. **(C)** Zeta potential of Ni-MOF and Ni/Cd-MOF at different pH.

conducted, as shown in **Figure 7A**. Obviously, the adsorption capacity increased sharply within 60 min and approached adsorption equilibrium within 240 min, achieving 81.1% removal rate of Pb(II) by Ni/Cd-MOF and 40.1% by Ni-MOF. Typical pseudo-first and pseudo-second kinetic models were used to fit the kinetic curves with the corresponding parameters listed in **Table 1**. The psuedo-second-order model presents a better fit with a higher regression coefficient of R^2 (0.9870 for Ni-MOF and 0.9938 for Ni/Cd-MOF), which reveals that chemisorption plays a leading role in the process of Pb^{2+} adsorption onto 2D MOFs. Comparing the two 2D MOF samples, we can find that bimetallic Ni/Cd-MOF shows a much higher rate parameter K_2 of 6.76 $\times 10^{-3}$ mg/(g h) than monometallic Ni-MOF [1.88×10^{-3} mg/(g h)], indicating that Ni/Cd-MOF with a larger pore size and less layer stacking renders a faster diffusion of Pb^{2+} to its active sites.

The Weber–Morris model was used to further explain the diffusion mechanism (**Table 2**). Multi-linear plots in **Figure 7B** illustrate that three adsorption processes including external surface adsorption, intraparticle diffusion, and adsorption equilibrium exist during Pb^{2+} capture onto the two 2D MOF samples (Doke and Khan, 2017). Among them, the first linear part is attributed to the heavy metal ions reaching the outer surface of the adsorbent through solution diffusion. During this diffusion process, Ni/Cd-MOF has a more negative charged surface and has a stronger electrostatic attraction for Pb^{2+} capture, displaying a higher adsorption rate of K_a [192.01 mg/(g $min^{0.5}$)] than Ni-MOF [176.52 mg/(g $min^{0.5}$)]. The second linear segment is assigned to the diffusion inside particles, and the bimetallic Ni/Cd-MOF has a larger pore size and less stacking layers, which efficiently reduces the diffusion resistance for Pb^{2+} adsorption and shows a significantly higher adsorption rate of K_b. The third stage is adsorption equilibrium (Skrzypczak et al., 2019; Tu et al., 2020). Therefore, Ni/Cd-MOF with a higher surface area, larger pore size, higher surface negativity, and less π-π stacking achieved a rapid diffusion of Pb^{2+} to its active sites and reflected its higher adsorption rate for Pb^{2+} removal.

In addition, the adsorption capacity of the as-prepared 2D MOFs was evaluated *via* the adsorption isotherm experiment without any solution pH adjusting. The results are shown in **Figures 7C,D**, which are fitted by four typical isotherm models of Langmuir, Freundlich, Redlich–Peterson, and Dubinin–Ashtakhov, and their fitting parameters are listed in **Table 3**. The results showed that the Redlich–Peterson model with higher regression coefficients gave an exponent β value close to 1, which indicates that Pb^{2+} adsorption onto 2D MOFs was ascribed to monolayer adsorption in accordance with the ideal Langmuir condition. The obtained saturated adsorption amount (Q_0) of Ni/Cd-MOF from the Langmuir model is as high as 950.61 mg/g, which is almost twice the Q_0 (522.94 mg/g) of monometallic Ni-MOF. Such appealing adsorption capacity of bimetallic Ni/Cd-MOF is quite superior over most of the other adsorbents reported for Pb^{2+} removals, such as MXene, graphene oxide composites, NH_2-Zr-MOF, and ED-MIL-101, as displayed in **Supplementary Table S2**. K_d value, an indicator of the affinity of adsorbent toward adsorbate in solution, was calculated at different equilibrium concentrations, and the resulted K_d plots

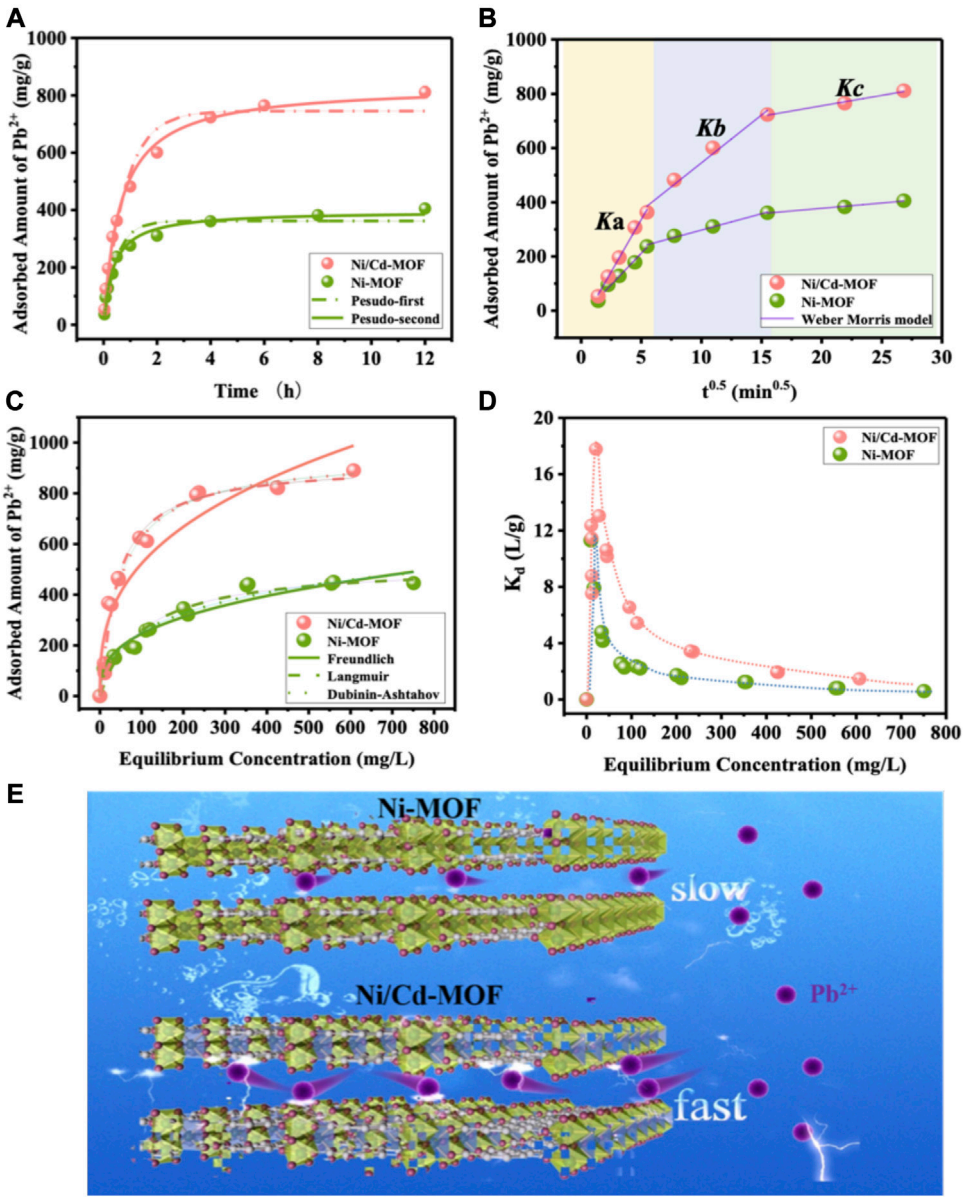

FIGURE 7 | (A) Adsorption kinetic curves of Pb^{2+} onto Ni-MOF and Ni/Cd-MOF, and their corresponding model fitting curves (equilibrium pH: ~5.1 without any adjustment); **(B)** diffusion model fitting curves of Pb^{2+} on Ni-MOF and Ni/Cd-MOF; **(C)** adsorption isotherms of Pb^{2+} onto Ni-MOF and Ni/Cd-MOF, and four model fitting curves; **(D)** the variation in the partition coefficient (K_d) with the equilibrium concentration for the adsorption of Pb^{2+} onto Ni-MOF and Ni/Cd-MOF; **(E)** schematic diagram of different adsorption behaviors of Pb^{2+} onto Ni-MOF and Ni/Cd-MOF.

TABLE 1 | Regression parameters of kinetic models for Pb^{2+} adsorption on two different MOFs.

Sample	Pseudo-first-order model[a]			Pseudo-second-order model[b]		
	Qe (mg/g)	K1 (/h)	R^2	Q_e (mg/g)	K2 [mg/(g h)]	R^2
Ni/MOF	362.1 ± 16.1	1.25 ± 0.18	0.9450	396.7 ± 9.9	1.88×10^{-3} ± 0.18×10^{-3}	0.9870
Ni-Cd/MOF	745.3 ± 30.5	2.05 ± 0.33	0.9650	835.4 ± 17.7	6.76×10^{-3} ± 0.84×10^{-3}	0.9938

[a]*The pseudo-first-order model:* $Q_t = Q_e(1 - e^{-K_1 t})$.

[b]*The pseudo-second-order model:* $Q_t = \frac{K_2 Q_e^2 t}{1+K_2 Q_e t}$, Q_t *is the amount sorbed per unit weight of sorbent at* t *time, mg/g;* t *is the time;* Q_e *(mg/g) is the adsorption capacity coefficient at equilibrium time;* K_1 *(/h) and* K_2 *[mg/ (g h)] are the rate constants;* R^2 *is the regression coefficient.*

TABLE 2 | Weber Morris model fitting curves of Pb^{2+} adsorption onto two different MOFs.

Sample	K_a [mg/(g $min^{0.5}$)]	R^2	K_b [mg/(g $min^{0.5}$)]	R^2	K_c [mg/(g $min^{0.5}$)]	R^2
Ni-MOF	176.52 ± 8.87	0.9904	46.45 ± 3.08	0.9870	3.91 ± 0.40	0.9898
Ni/Cd-MOF	192.01 ± 3.86	0.9791	77.21 ± 2.98	0.9956	7.69 ± 0.78	0.9796

Weber Morris model: $Q_t = K_i t^{0.5} + C$, Q_t *is the amount sorbed per unit weight of sorbent at* t *time, mg/g;* K_i *is the diffusion rate constant during different stages, mg/g·*$min^{0.5}$*;* t *is the time, min;* C *is a constant; and* R^2 *is the regression coefficient.*

are presented in **Figure 7D**. Both the samples' K_d plots undergo an up and downtrend, and apparently bimetallic Ni/Cd-MOF showed a much higher affinity for Pb^{2+} adsorption during the full range of equilibrium concentration, which possessed significantly higher K_d values than monometallic Ni-MOF. What is more, the maximum point of Ni/Cd-MOF's K_d value occurred at a higher equilibrium concentration than that of Ni-MOF, which means bimetallic Ni/Cd-MOF can exhibit its high affinity for Pb^{2+} capture even in a solution with a high concentration of Pb^{2+}. The high-affinity property of Ni/Cd-MOF toward Pb^{2+} was further supported by the fitting parameter of Langmuir *b*, another indicator of the adsorption affinity, and the *b* value calculated for Ni/Cd-MOF (0.0192 L/mg) is twice over that for Ni-MOF (0.0097 L/mg). The characteristic adsorption energy of *E* was calculated to 26.40 kJ/mol of Ni/Cd-MOF from the Dubinin–Ashtahov model, ~8 kJ/mol higher than that of Ni-MOF (18.51 kJ/mol), similarly indicating the higher interaction strength of bimetallic Ni/Cd-MOF for Pb^{2+} adsorption. Consequently, the above analysis based on adsorption isotherm curves proved that bimetallic Ni/Cd-MOF presents obviously high adsorption capacity and adsorption affinity for Pb^{2+} removal as shown in **Figure 7E**.

Selective Adsorption Behaviors

A mixed solution containing four heavy metal ions (Co^{2+}, Fe^{3+}, Cu^{2+}, and Pb^{2+}) was used to test the selective adsorption capacity of 2D Ni-based MOFs. Among them, the metal ion concentration was set to 50 mg/L, and the adsorption efficiency rate is shown in **Figure 8**. The adsorption ability of both Ni-MOF and Ni/Cd-MOF toward Pb^{2+} was noticeably higher than that toward Co^{2+}, Fe^{3+}, and Cu^{2+}.

Mechanism of Pb^{2+} Adsorption Onto 2D MOFs

To gain a rational understanding of the interaction mechanism of Pb^{2+} adsorption onto 2D MOFs, element states and chemical bonds of two samples before and after Pb^{2+} adsorption were analyzed by FTIR and XPS, respectively. In the FTIR spectra (**Figures 9A,B**), the intensity ratio of the band at 1,577 cm^{-1} for –COO– (ν_{as}) relative to the band at 815 cm^{-1} for C–H on the benzene ring (γ) was used as a spectroscopic indicator of the coordinated condition in the 2D MOF structure. The value of the ν_{as}(–COO–)/γ(C–H) ratio increased from 1.85 to 2.01 for Ni-MOF and from 2.02 to 2.42 for Ni/Cd-MOF after Pb^{2+} adsorption, which soundly reveals that –COO– on 2D MOFs served as the main adsorption site for Pb^{2+} capture *via*

TABLE 3 | Freundlich, Langmuir, and Dubinin–Ashtahov regression parameters of Pb^{2+} adsorption isotherms onto two different MOFs.

Sample	Freundlich[a]			Langmuir[b]			Redlich–Peterson[c]				Dubinin–Ashtahov[d]			
	N	Kf	R^2	Q^o (mg/g)	*b* (L /mg)	R^2	KR (L/g)	α (L/mg)	β	R^2	Qo (mg/g)	E (KJ/mol)	n	R^2
Ni-MOF	0.3427 ± 0.0262	50.68 ± 7.86	0.9563	522.94 ± 24.58	0.0097 ± 0.0015	0.9557	6.06 ± 2.05	0.020 ± 0.023	0.9167 ± 0.13	0.9660	538.97 ± 18.61	18.51 ± 1.41	2.48 ± 0.95	0.9659
Ni/Cd-MOF	0.3529 ± 0.0400	102.91 ± 22.79	0.9079	950.61 ± 32.51	0.0192 ± 0.0024	0.9784	16.78 ± 2.2	0.029 ± 0.0039	0.9467 ± 0.07	0.9791	909.39 ± 40.90	26.40 ± 0.28	7.15 ± 0.85	0.9852

[a] *The Freundlich model:* $Q = K_f C_e^{\ N}$.

[b] *The Langmuir model:* $Q = Q_{ob}C_e/(1+_bC_e)$.

[c] *The Redlich–Peterson model:* $Q_e = K_R C_e/(1 + \alpha C_e^{\beta})$.

[d] *The Dubinin–Ashtahov model:* $logQ = logQ_o - (\varepsilon/E)^n$, *Q is the amount sorbed per unit weight of sorbent, mg/g;* C_e *is the equilibrium concentration, mg/L;* K_f *[(mg/kg)/(mg/L)*^{N}*] is the Freundlich capacity coefficient;* N *is the isotherm curvature;* Q^o *(mg/g) is the adsorption capacity coefficient; and* b *(L/mg) is the adsorption rate coefficient;* K_R *and* α *are the Redlich–Peterson isotherm constants, and* β *is the exponent (0< β< 1);* ε *(kJ/mol),* $\varepsilon = RTln(C_e/C_s)$*, is the effective adsorption potential;* C_s *(mg/L) is the water solubility of* Pb^{2+}*.*Pb^{2+} *(353434 mg/L);* $R = 8.314\times10^{-3}$ *kJ/(mol·K) is the universal gas constant; T (K) is the absolute temperature;* E *(kJ/mol) is the characteristic energy of adsorption; and n and* R^2 *are fitting parameters.*

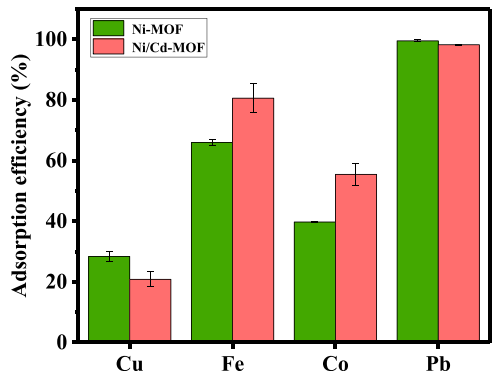

FIGURE 8 | The adsorption of various heavy metals ions by Ni-MOF and Ni/Cd-MOF.

Furthermore, XPS analysis was conducted to investigate the variation in atomic valence and chemical bonds of Ni-based MOFs before and after the adsorption of Pb(II). According to the full XPS spectra in **Figures 9C,D, a** new bimodal pattern Pb 4f can be obviously observed around 139 eV on both Ni-MOF and Ni/Cd-MOF after adsorption compared to virgin adsorbents. This indicated the presence of Pb(II) on the Ni-based MOF nanosheets. Importantly, O mainly from the −COO on the organic linker, as the key coordination sites for metal ions in 2D MOFs, was further determined in terms of its high-resolution O1 spectra, and the corresponding peak-differentiating results are presented in **Figures 9E–H**. Three individual peaks can be deconvoluted at 531.3, 532.4, and 533.4 eV, which are assigned to metal−O-C/O=C (coordinated state), O-C/O=C (uncoordinated state), and O from structural water, respectively. Although there is no significant difference in the

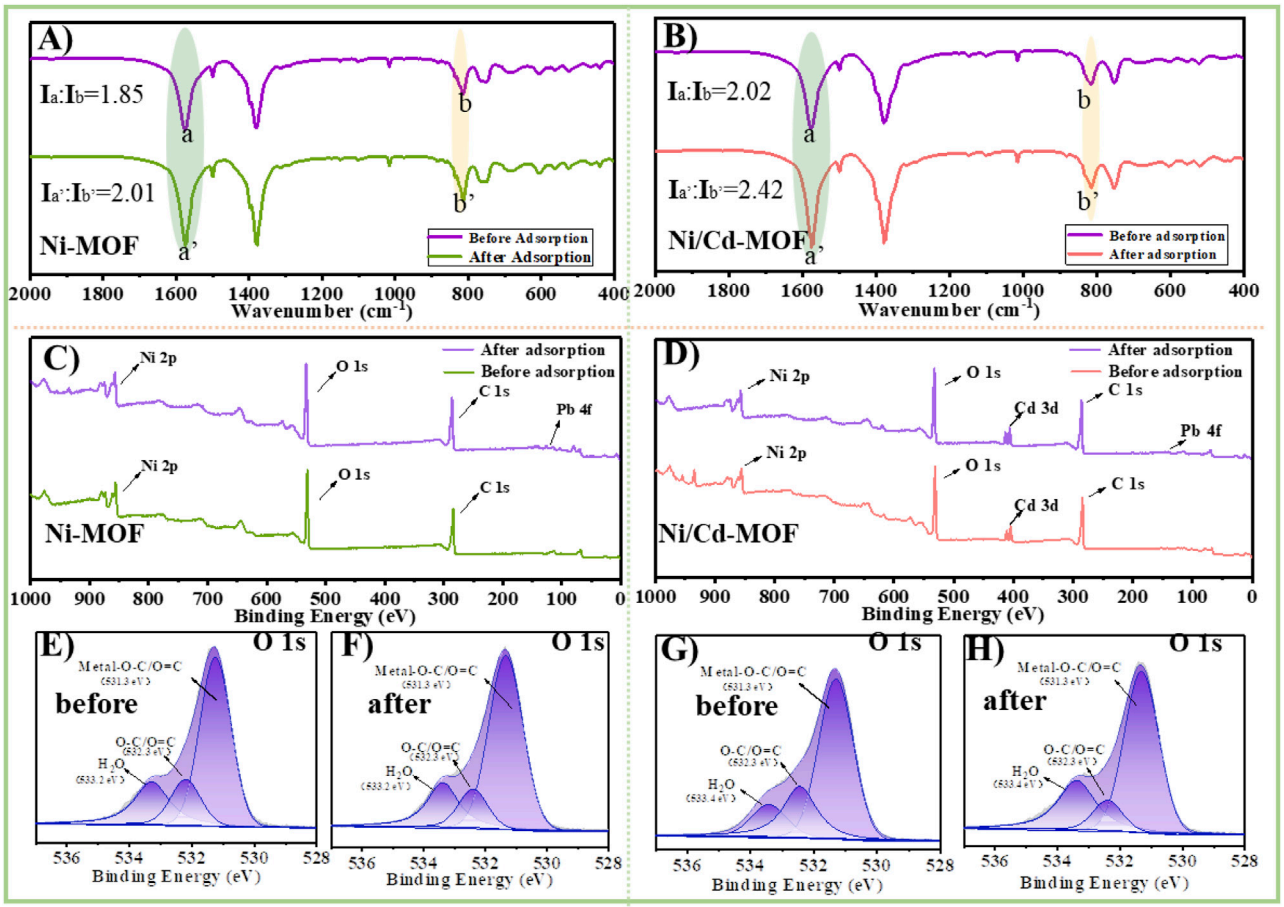

FIGURE 9 | FTIR spectra of **(A)** Ni-MOF and **(B)** Ni/Cd-MOF before and after Pb^{2+} adsorption. XPS full spectra of **(C)** Ni-MOF and **(D)** Ni/Cd-MOF before and after Pb^{2+} adsorption. High-resolution XPS O1 spectra **(E)** before and **(F)** after Pb^{2+} adsorption on Ni-MOF. High-resolution XPS O1 spectra **(G)** before and **(H)** after Pb^{2+} adsorption on Ni/Cd-MOF.

coordination interaction, whose intensity significantly increased after Pb^{2+} adsorption on both of monometallic Ni-MOF and bimetallic Ni/Cd-MOF.

proportion of O in the coordinated state or uncoordinated state between Ni-MOF and Ni/Cd-MOF, after Pb^{2+} adsorption, their changes are very inconsistent. The proportion of O in the

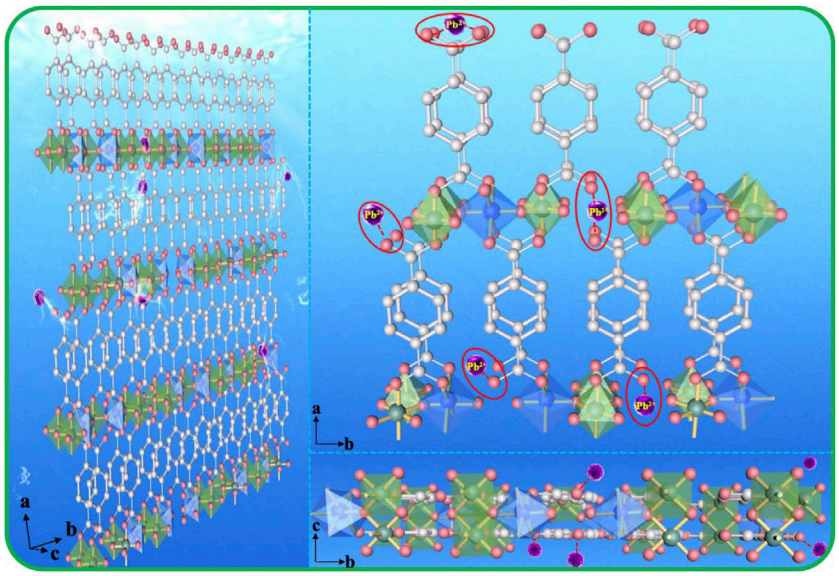

FIGURE 10 | Schematic diagram of 2D MOFs for Pb^{2+} removal in aqueous solution.

coordinated state increased from 59.5 to 61.2% of Ni-MOF after Pb^{2+} adsorption, with 1.7% increase; accordingly, the proportion of O in the uncoordinated state decreased. However, the proportion of O in the coordinated state increased from 58.8 to 64.4% of bimetallic Ni/Cd-MOF, which is a 5.6% increase—significantly higher than monometallic Ni-MOF, and similarly, the proportion of O in the uncoordinated state showed a remarkable decline. The above results further confirm that the −COO from organic linker on 2D MOFs are the main adsorption sites for Pb^{2+} coordination, and bimetallic Ni/Cd-MOF has more active −COO sites for Pb^{2+} binding. Therefore, the adsorption mechanism and application process of 2D MOFs prepared here for solution Pb^{2+} removal are graphically illustrated in **Figure 10**; it is easier for hydrated heavy metal ions to access the internal and surface active sites of Ni/Cd-MOF nanosheets due to its lager layer spacing than Ni-MOF, and meanwhile, the strong binding ability of uncoordinated -COO- enabled Ni/Cd-MOF nanosheets has the higher adsorption for Pb(II).

CONCLUSION

In summary, 2D MOF nanosheets were successfully fabricated *via* a one-step mixed-solvent solvothermal method without recourse to a common exfoliation process. Metal inorganic cluster regulation in the 2D MOFs was realized by bimetallic coordination, which significantly enhanced Pb^{2+} adsorption. Binary metal coordination rendered more crystal defects and vacancies in the framework derived from the lattice distortion or locally unbalanced coordination. Thus, compared to monometallic Ni-MOF, bimetallic Ni/Cd-MOF exhibited fewer layers (4~5 layers), higher specific surface area, larger pore size, and higher surface electronegativity, which lead to rapid diffusion of Pb^{2+} to its active sites, reflecting its high adsorption rate and high adsorption capacity (950.61 mg/g, almost twice as high as that of monometallic Ni-MOF) for Pb^{2+} removal. Adsorption kinetic fitting revealed that Pb^{2+} adsorption onto the 2D MOFs experienced external surface adsorption, intraparticle diffusion, and adsorption equilibrium stages. It is inferred that the uncoordinated carboxyl groups (−COO−) in 2D MOFs dominated the adsorption, and binary metal regulation in 2D MOFs created more uncoordinated −COO− groups for Pb^{2+} adsorption. The present work provides a promising regulation strategy based on bimetallic coordination of 2D MOFs to realize highly efficient adsorption removal of heavy metal ions.

DATA AVAILABILITY STATEMENT

The original contributions presented in the study are included in the article/**Supplementary Material**; further inquiries can be directed to the corresponding authors.

AUTHOR CONTRIBUTIONS

GL: formal analysis, investigation, writing—original draft, and writing—review. YL: investigation. YS: investigation, and review and editing. QF: writing—review and editing, and supervision. FL: funding acquisition, writing—review and editing, and supervision.

FUNDING

This work was kindly supported by the National Natural Science Foundation of China (51673209, 51973230), Zhejiang Provincial Natural Science Foundation of China for Distinguished Young

Scholars (LR20E030002), Ten thousand plan: high-level talents special support plan of Zhejiang Province, China (ZJWR0108020), Youth Innovation Promotion Association of Chinese Academy of Science (2014258), and Ningbo Municipal Bureau of Science and Technology (2019C50028).

SUPPLEMENTARY MATERIAL

The Supplementary Material for this article can be found online at: https://www.frontiersin.org/articles/10.3389/fceng.2021.636439/full#supplementary-material.

REFERENCES

Abednatanzi, S., Derakhshandeh, P. G., Depauw, H., Coudert, F., Vrielinck, H., Van Der Voort, P., et al. (2019). Mixed-metal metal-organic frameworks. *Chem. Soc. Rev.* 48, 2535–2565. doi:10.1039/C8CS00337H

Alyüz, B., and Veli, S. (2009). Kinetics and equilibrium studies for the removal of nickel and zinc from aqueous solutions by ion exchange resins. *J. Hazard. Mater.* 167, 482–488. doi:10.1016/j.jhazmat.2009.01.006

Caglayan, B., and Aksoylu, A. E. (2013). CO2 adsorption on chemically modified activated carbon. *J. Hazard. Mater.* 252-253, 19–28. doi:10.1016/j.jhazmat.2013.02.028

Cai, M., Liu, Q., Xue, Z., Li, Y., Fan, Y., Huang, A., et al. (2020). Constructing 2D MOFs from 2D LDHs: highly efficient and durable electrocatalyst for water oxidation. *J. Mater. Chem. A.* 8, 190–195. doi:10.1039/C9TA09397D

Chen, C., and Wang, X. (2006). Adsorption of Ni(II) from aqueous solution using oxidized multi-walled carbon nanotubes. *Ind. Eng. Chem. Res.* 45, 9144–9149. doi:10.1021/ie060791z

Chen, D., Shen, W., Wu, S., Chen, C., Luo, X., and Guo, L. (2016). Ion exchange induced removal of Pb(II) by MOF-derived magnetic inorganic sorbents. *Nanoscale* 8, 7172–7179. doi:10.1039/C6NR00695G

Cliffe, M. J., Castillo-Martínez, E., Wu, Y., Lee, J., Forse, A. C., Firth, F. C. N., et al. (2017). Metal-organic nanosheets formed via defect-mediated transformation of a hafnium metal-organic framework. *J. Am. Chem. Soc.* 139, 5397–5404. doi:10.1021/jacs.7b00106

Dhakshinamoorthy, A., Asiri, A. M., and Garcia, H. (2019). 2D metal-organic frameworks as multifunctional materials in heterogeneous catalysis and electro/photocatalysis. *Adv. Mater.* 31, 1900617. doi:10.1002/adma.201900617

Doke, K. M., and Khan, E. M. (2017). Equilibrium, kinetic and diffusion mechanism of Cr(VI) adsorption onto activated carbon derived from wood apple shell. *Arab. J. Chem.* 10, S252–S260. doi:10.1016/j.arabjc.2012.07.031

Du, J., Xu, S., Sun, L., and Li, F. (2019). Iron carbonate hydroxide templated binary metal-organic frameworks for highly efficient electrochemical water oxidation. *Chem. Commun.* 55, 14773. doi:10.1039/C9CC07433C

Duan, S., Wu, L., Li, J., Huang, Y., Tan, X., Wen, T., et al. (2019). Two-dimensional copper-based metal-organic frameworks nano-sheets composites: one-step synthesis and highly efficient U(VI) immobilization. *J. Hazard. Mater.* 373, 580–590. doi:10.1016/j.jhazmat.2019.03.119

Fu, F., and Wang, Q. (2011). Removal of heavy metal ions from wastewaters: a review. *J. Environ. Manage.* 92, 407–418. doi:10.1016/j.jenvman.2010.11.011

Howarth, A. J., Katz, M. J., Wang, T. C., Platero-Prats, A. E., Chapman, K. W., Hupp, J. T., et al. (2015). High efficiency adsorption and removal of selenate and selenite from water using metal-organic frameworks. *J. Am. Chem. Soc.* 137, 7488–7494. doi:10.1021/jacs.5b03904

Jafari, Z., Avargani, V., Rahimi, M., and Mosleh, S. (2020). Magnetic nanoparticles-embedded nitrogen-doped carbon nanotube/porous carbon hybrid derived from a metal-organic framework as a highly efficient adsorbent for selective removal of Pb(II) ions from aqueous solution. *J. Mol. Liq.* 318, 113987. doi:10.1016/j.molliq.2020.113987

Jian, M., Wang, H., Liu, R., Qu, J., Wang, H., and Zhang, X. (2016). Self-assembled one-dimensional MnO_2@zeolitic imidazolate framework-8 nanostructures for highly efficient arsenite removal. *Environ. Sci. Nano.* 3, 1186–1194. doi:10.1039/C6EN00246C

Jiang, D., Chen, M., Wang, H., Zeng, G., Huang, D., Cheng, M., et al. (2019). The application of different typological and structural MOFs-based materials for the dyes adsorption. *Coord. Chem. Rev.* 380, 471–483. doi:10.1016/j.ccr.2018.11.002

Lei, C., Gao, J., Ren, W., Xie, Y., Abdalkarim, S., Wang, S., et al. (2019). Fabrication of metal-organicframeworks@celluloseaerogels composite materials for removal of heavy metal ions in water. *Carbohyd. Polym.* 205, 35–41. doi:10.1016/j.carbpol.2018.10.029

Li, B., Wen, H., Cui, Y., Zhou, W., Qian, G., and Chen, B. (2016). Emerging multifunctional metal-organic framework materials. *Adv. Mater.* 28, 8819–8860. doi:10.1002/adma.201601133

Li, F., Wang, P., Huang, X., Young, D., Wang, H., Braunstein, P., et al. (2019a). Large-scale, bottom-up synthesis of binary metal-organic framework nanosheets for efficient water oxidation. *Angew. Chem. Int. Ed.* 131, 7125–7130. doi:10.1002/ange.201902588

Li, G., Ye, J., Fang, Q., and Liu, F. (2019b). Amide-based covalent organic frameworks materials for efficient and recyclable removal of heavy metal lead (II). *Chem. Eng. J.* 370, 822–830. doi:10.1016/j.cej.2019.03.260

Li, J., Wang, X., Zhao, G., Chen, C., Chai, Z., Alsaedi, A., et al. (2018). Metal-organic framework-based materials: superior adsorbents for the capture of toxic and radioactive metal ions. *Chem. Soc. Rev.* 47, 2322–2356. doi:10.1039/C7CS00543A

Liu, X., Jiang, B., Yin, X., Ma, H., and Hsiao, B. (2020). Highly permeable nanofibrous composite microfiltration membranes for removal of nanoparticles and heavy metal ions. *Sep. Purif. Technol.* 233, 115976. doi:10.1016/j.seppur.2019.115976

Luo, B., Yuan, L., Chai, Z., Shi, W., and Tang, Q. (2016). U(VI) capture from aqueous solution by highly porous and stable MOFs: UiO-66 and its amine derivative. *J. Radioanal. Nucl. Chem.* 307, 269–276. doi:10.1007/s10967-015-4108-3

Luo, F., Chen, J. L., Dang, L. L., Zhou, W. N., Lin, H. L., Li, J. Q., et al. (2015a). High-performance Hg^{2+} removal from ultra-low-concentration aqueous solution using both acylamide- and hydroxyl-functionalized metal-organic framework. *J. Mater. Chem. A.* 3, 9616–9620. doi:10.1039/C5TA01669J

Luo, X., Ding, L., and Luo, J. (2015b). Adsorption removal of Pb(II) ions from aqueous samples with amino-functionalization of metal-organic frameworks MIL-101(Cr). *J. Chem. Eng. Data* 60, 1732–1743. doi:10.1021/je501115m

Masoomi, M. Y., Morsali, A., Dhakshinamoorthy, A., and Garcia, H. (2019). Mixed-metal MOFs: unique opportunities in metal-Organic framework (MOF) functionality and design. *Angew. Chem. Int. Ed.* 58, 15188–15205. doi:10.1002/anie.201902229

Matlock, M., and Howerton, B. (2002). Atwood, and D. AChemical precipitation of lead from lead battery recycling plant wastewater. *Ind. Eng. Chem. Res.* 41, 1579–1582. doi:10.1021/ie010800y

Meng, Z., Luo, J., Li, W., and Mirica, K. A. (2020). Hierarchical tuning of the performance of electrochemical carbon dioxide reduction using conductive two-dimensional metallophthalocyanine based metal-organic frameworks. *J. Am. Chem. Soc.* 142, 21656–21669. doi:10.1021/jacs.0c07041

Naseem, R., and Tahir, S. S. (2001). Removal of Pb(II) from aqueous solution by using bentonite as an adsorbent. *Water Res.* 35, 3982–3986. doi:10.1016/S0043-1354(01)00130-0

Pang, W., Shao, B., Tan, X., Tang, C., Zhang, Z., and Huang, J. (2020). Exfoliation of metal-organic frameworks into efficient single-layer metal-organic nanosheet electrocatalysts by the synergistic action of host-guest interactions and sonication. *Nanoscale* 12, 3623–3629. doi:10.1039/C9NR09742B

Peng, Y., Li, Y., Ban, Y., Jin, H., Jiao, W., Liu, X., et al. (2014). Membranes. Metal-organic framework nanosheets as building blocks for molecular sieving membranes. *Science* 346, 1356–1359. doi:10.1126/science.1254227

Skrzypczak, D., Witek-Krowiak, A., Dawiec-Lisniewska, A., Podstawczyk, D., Mikula, K., and Chojnacka, K. (2019). Immobilization of biosorbent in hydrogel as a new environmentally friendly fertilizer for micronutrients delivery. *J. Clean. Prod.* 241, 118387. doi:10.1016/j.jclepro.2019.118387

Tu, B., Wen, R., Wang, K., Cheng, Y., Deng, Y., Cao, W., et al. (2020). Efficient removal of aqueous hexavalent chromium by activated carbon derived from Bermuda grass. *J. Colloid. Interf. Sci.* 560, 649–658. doi:10.1016/j.jcis.2019.10.103

Uzunova, E., Klissurski, D., and Kassabov, S. (1994). Nickel-iron hydroxide carbonate precursors in the synthesis of high-dispersity oxides. *J. Mater. Chem.* 4, 153–159. doi:10.1039/JM9940400153

Vuong, G. T., Pham, M. H., and Do, T. O. (2013). Synthesis and engineering porosity of a mixed metal Fe2Ni MIL-88B metal-organic framework. *Dalton Trans.* 42, 550–557. doi:10.1039/C2DT32073H

Wang, N., Mundstock, A., Liu, Y., Huang, A., and Caro, J. (2015). Amine-modified Mg-MOF-74/CPO-27-Mg membrane with enhanced H_2/CO_2 separation. *Chem. Eng. J.* 124, 27–36. doi:10.1016/j.ces.2014.10.037

Wen, Z., Ke, J., Xu, J., Guo, S., Zhang, Y., and Chen, R. (2018). One-step facile hydrothermal synthesis of flowerlike Ce/Fe bimetallic oxides for efficient As(V) and Cr(VI) remediation: performance and mechanism. *Chem. Eng. J.* 343, 416–426. doi:10.1016/j.cej.2018.03.034

Xu, L., Wang, Y., Xu, T., Liu, S., Tong, J., Chu, R., et al. (2018). Exfoliating polyoxometalate-encapsulating metal-organic framework into two-dimensional nanosheets for superior oxidative desulfurization. *ChemCatChem* 10, 5386–5390. doi:10.1002/cctc.201801495

Xu, R., Jiand, M., Jia, Q., Hu, C., Tang, C., Liu, R., et al. (2020). 2D water-stable zinc-benzimidazole framework nanosheets for ultrafast and selective removal of heavy metals. *Chem. Eng. J.* 382, 122658. doi:10.1016/j.cej.2019.122658

Yan, Y., Li, C., Wu, Y., Gao, J., and Zhang, Q. (2020). From isolated Ti-oxo clusters to infinite Ti-oxo chains and sheets: recent advances in photoactive Ti-based MOFs. *J. Mater. Chem. A.* 8, 15245–15270. doi:10.1039/D0TA03749D

Yang, S., Hu, J., Chen, C., Shao, D., and Wang, X. (2011). Mutual effects of Pb(II) and humic acid adsorption on multiwalled carbon nanotubes/polyacrylamide composites from aqueous solutions. *Environ. Sci. Technol.* 45, 3621–3627. doi:10.1021/es104047d

Yang, Z., Cao, J., Chen, Y., Li, X., Xiong, W., Zhou, Y., et al. (2019). Mn-doped zirconium metal-organic framework as an effective adsorbent for removal of tetracycline and Cr(VI) from aqueous solution. *Microp. Mesopor. Mater.* 277, 277–285. doi:10.1016/j.micromeso.2018.11.014

Zhang, B., Qiu, W., Wang, P., Liu, Y., Zou, J., Wang, L., et al. (2020). Mechanism study about the adsorption of Pb(II) and Cd(II) with iron-trimesic metal-organic frameworks. *Chem. Eng. J.* 385, 123507. doi:10.1016/j.cej.2019.123507

Zhang, T., Wang, J., Zhang, W., Yang, C., Zhang, L., Zhu, W., et al. (2019). Amorphous Fe/Mn bimetal-organic frameworks: outer and inner structural designs for efficient arsenic (III). *J. Mater. Chem. A.* 7, 2845–2854. doi:10.1039/C8TA10394A

Zhao, M., Huang, Y., Peng, Y., Huang, Z., Ma, Q., and Zhang, H. (2018). Two-dimensional metal-organic framework nanosheets: synthesis and applications. *Chem. Sov. Rev.* 47, 6267–6295. doi:10.1039/C8CS00268A

Conflict of Interest: The authors declare that the research was conducted in the absence of any commercial or financial relationships that could be construed as a potential conflict of interest.